Chinese Chemical Letters 34 (2023) 107585

Contents lists available at ScienceDirect

Chinese Chemical Letters

journal homepage: www.elsevier.com/locate/cclet

Enhanced macrophage polarization induced by COX-2 inhibitor-loaded Pd octahedral nanozymes for treatment of atherosclerosis

Min Xu[a], Chuchu Ren[a], Yue Zhou[a], Zbynek Heger[b], Xiaoyang Liang[a], Vojtech Adam[b,*], Nan Li[a,*]

[a] School of Pharmaceutical Science and Technology, Tianjin University, Tainjin 300072, China
[b] Department of Chemistry and Biochemistry, Mendel University in Brno, Brno CZ-613 00, Czech Republic

ARTICLE INFO

Article history:
Received 12 November 2021
Revised 1 June 2022
Accepted 5 June 2022
Available online 10 June 2022

Keywords:
Atherosclerosis
COX-2 inhibitor
Pd octahedral nanozyme
Macrophage polarization
Anti-inflammation
Antioxidation

ABSTRACT

Inhibition of foam cell formation is considered a promising treatment method for atherosclerosis, the leading cause of cardiovascular diseases worldwide. However, currently available therapeutic strategies have shown unsatisfactory clinical outcomes. Thus, herein, we design aloperine (ALO)-loaded and hyaluronic acid (HA)-modified palladium (Pd) octahedral nanozymes (Pd@HA/ALO) that can synergistically scavenge reactive oxygen species (ROS) and downregulate cyclooxygenase-2 (COX-2) expression to induce macrophage polarization, thus inhibiting foam cell formation to attenuate atherosclerosis. Due to the targeted effect of HA on stabilin-2 and CD44, which are overexpressed in atherosclerotic plaques, Pd@HA/ALO can actively accumulate in atherosclerotic plaques. Subsequently, the antioxidative effects of Pd octahedral nanozymes are mediated by their intrinsic superoxide dismutase- and catalase-like activities capable of effective scavenging of ROS. In addition, anti-inflammatory effects are mediated by controlled, on-demand near-infrared-triggered ALO release leading to inhibition of COX-2 expression. Importantly, the combined therapy can promote the polarization of macrophages to the M2 subtype by upregulating Arg-1 and CD206 expression and downregulating expression of TNF-α, IL-1β and IL-6, thereby inhibiting atherosclerosis-related foam cell formation. In conclusion, the presented *in vitro* and *in vivo* data demonstrate that Pd@HA/ALO enhanced macrophage polarization to reduce plaque formation, identifying an attractive treatment strategy for cardiovascular disease.

Atherosclerosis, which is characterized by chronic inflammation of the arterial wall, is a major contributor to cardiovascular diseases and remains the leading cause of morbidity and mortality in industrialized countries [1,2]. Lipid-regulating drugs are the primary treatment for atherosclerosis, but long-term disease remission is not achieved due to the adverse side effects [3–5]. Other small molecule drugs, such as probucol, aspirin and indomethacin, have been widely used for the management of atherosclerosis [6–9]. Unfortunately, these therapies are limited to mildly delaying the progression of atherosclerosis due to the nonspecific distribution throughout the body. Currently, studies have shown that macrophages play a crucial role in the development of atherosclerosis [10]. In particular, different phenotypes of macrophages, including the proinflammatory classic (M1) and anti-inflammatory (M2) phenotypes, were found to affect the stability of atherosclerotic plaques [11–14]. M1 macrophages are predominant during the formation of atherosclerosis, inducing inflammation by secreting proinflammatory cytokines such as tumor necrosis factor-α (TNF-α), interleukin-1β (IL-1β) and interleukin-6 (IL-6) [15,16]. In contrast, M2 macrophages produce anti-inflammatory cytokines and are associated with resolution of atherosclerosis [17]. Therefore, alteration of the macrophage phenotype may be a strategy for the atherosclerosis management.

Fortunately, anti-inflammatory strategies may effectively alter the balance of macrophage subtypes for treatment of atherosclerosis [18,19]. Recent studies have found that cyclooxygenase-2 (COX-2), a member of the COX family, plays an important role in the inflammatory response [20,21]. Interestingly, aloperine (ALO), an alkaloid extracted from *Sophora alopecuroides* L., have shown anti-inflammatory activity in both *in vivo* and *in vitro* settings [22]. As reported previously, ALO reduces the expression of COX-2, thereby exhibiting an anti-inflammatory effect and promoting the phenotypic transition of M1 macrophages to the M2 subtype, which is of utmost interest for atherosclerosis therapy [23]. However, it is

* Corresponding authors.
E-mail addresses: vojtech.adam@mendelu.cz (V. Adam), linan1985@tju.edu.cn (N. Li).

https://doi.org/10.1016/j.cclet.2022.06.008
1001-8417/

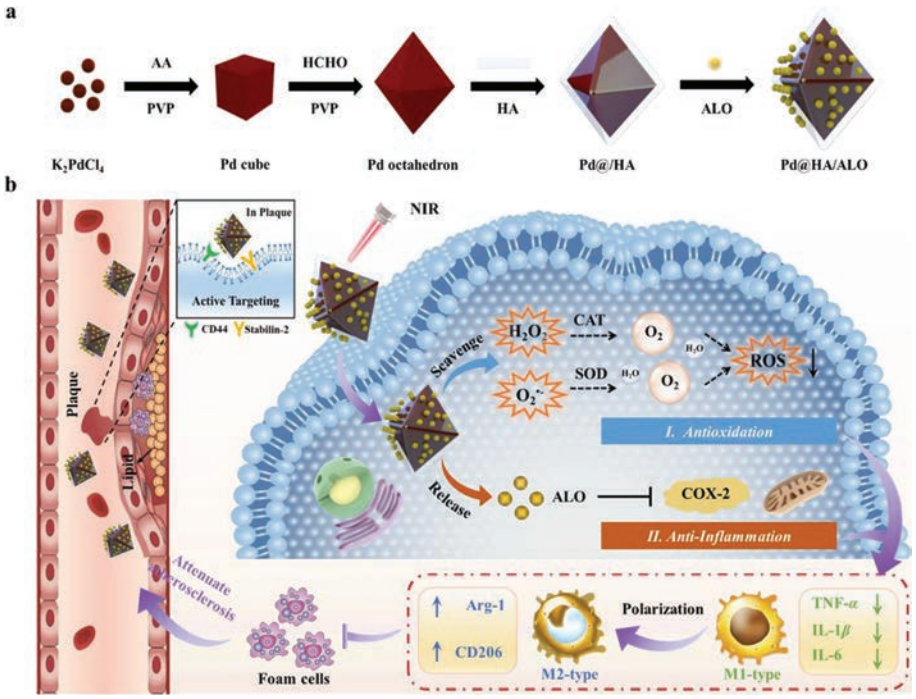

Scheme 1. Schematic illustration displaying (a) the preparation route of Pd@HA/ALO and (b) the therapeutic mechanism of Pd@HA/ALO in atherosclerosis treatment.

worth to note that efficient delivery of ALO to atherosclerotic lesions is notoriously difficult. Thus, ALO could substantially benefit from nanoparticle-based targeted delivery strategies that have been shown to provide major advantages (*e.g.,* improved bioavailability, efficacy and safety) not only in a therapy of cardiovascular-related diseases [24–28].

Recent studies have indicated that nanoparticles with intrinsic antioxidative activity are promising next-generation therapies for the treatment of atherosclerosis [29–31]. Specifically, through their antioxidative activity, these nanoparticles are able to regulate reactive oxygen species (ROS) for M1 to M2 phenotypic transition of macrophages, thus synergizing anti-inflammatory functions to effectively ameliorate atherosclerosis [32–35]. Notably, noble metal-based nanozymes, particularly palladium (Pd) nanoparticles, have received substantial interest due to their good biocompatibility and excellent antioxidative properties, such as catalase (CAT) and superoxide dismutase (SOD) activities [36–39]. More importantly, studies have shown that enzyme-like performance can be effectively adjusted by controlling the structure and crystal facets of Pd nanomaterials. In general, lower surface energy (111)-faceted Pd octahedrons have greater intrinsic antioxidative enzyme-like activities than higher surface energy (100)-faceted Pd nanocubes [40].

In this study, we designed ALO-loaded and hyaluronic acid (HA)-modified Pd octahedral nanozymes (Pd@HA/ALO) with synergistic antioxidative and anti-inflammatory activities to alleviate atherosclerosis through M1 to M2 polarization of macrophages (Scheme 1). The as-prepared Pd@HA/ALO nanoparticles were used to treat atherosclerosis through following multifactorial mechanism: (1) Pd@HA/ALO actively targets atherosclerotic plaques through HA-modified surface exhibiting affinity to stabilin-2 and CD44, which both are highly expressed in atherosclerotic plaques. (2) Pd octahedral nanozymes exert efficient SOD- and CAT-like activities, by which they scavenge multiple ROS and promote antioxidative treatment. (3) Under near-infrared (NIR) irradiation, ALO is released from Pd@HA/ALO, thus inhibiting the expression of COX-2 to exert an anti-inflammatory effect. (4) Synergistic antioxidative and anti- inflammatory effects promote the polarization of macrophages from the M1 to M2 subtype, thereby preventing the formation of foam cells to attenuate atherosclerosis. An array of comprehensive *in vitro* and *in vivo* experiments confirmed that the prepared nanozymes are able to prevent the progression of atherosclerosis and to stabilize atherosclerotic plaques.

The preparation process of Pd@HA/ALO is shown in Scheme 1a. First, Pd nanocubes were prepared based on a solution method using PVP, AA and KBr as a stabilizing agent, reductive agent and capping agent, respectively. The obtained Pd nanocubes exhibited uniform cubic shapes with average sizes of 32 nm, as confirmed by TEM (Fig. 1a). Next, the as-prepared Pd nanocubes were used as seeds to synthesize Pd octahedrons, demonstrated in the TEM micrograph (Fig. 1b). Specifically, Pd atoms were deposited on the (100) facet through thermodynamic control, leading to the transformation of Pd nanocubes into octahedra dominated by the (111) facet [41]. Finally, HA and ALO were subsequently adsorbed onto the surface to fabricate Pd@HA/ALO. This resulted in an increased particle size of ~50 nm (Fig. 1c). It is worth to note that dynamic light scattering revealed larger diameter (68.67 nm) compared to TEM micrographs. This was likely caused by the HA coating increasing the hydrodynamic diameter of Pd@HA/ALO (Fig. S1 in Supporting information). Moreover, the zeta potential decreased from -18.9 ± 0.6 mV (Pd octahedron) to −27.1 ± 1.15 mV (Pd@HA/ALO), indicating the successful coating of HA (Fig. S2 in Supporting information). In addition, the high-resolution TEM (HRTEM) micrographs (Figs. 1d and e) revealed lattice fringes of 0.20 and 0.22 nm, attributed to the (100) plane of the Pd nanocubes and the (111) plane of the Pd octahedrons, respectively. In addition, elemental mapping confirmed that Pd, O and N were homogeneously dispersed throughout the Pd@HA/ALO (Fig. 1f). Moreover, the powder XRD spectrum indicated preferential crystal growth along the (111) direction for the Pd octahedrons, which was consistent with the HRTEM results (Fig. 1g). In the XPS (Fig. 1h), the split energy between Pd $3d_{3/2}$ (341.1 eV) and Pd $3d_{5/2}$ (335.8 eV) was 5.3 eV, which indicated the existence of Pd^0 in the final products. The UV-vis spectra further showed that Pd@HA/ALO presented a broad absorption band from the UV

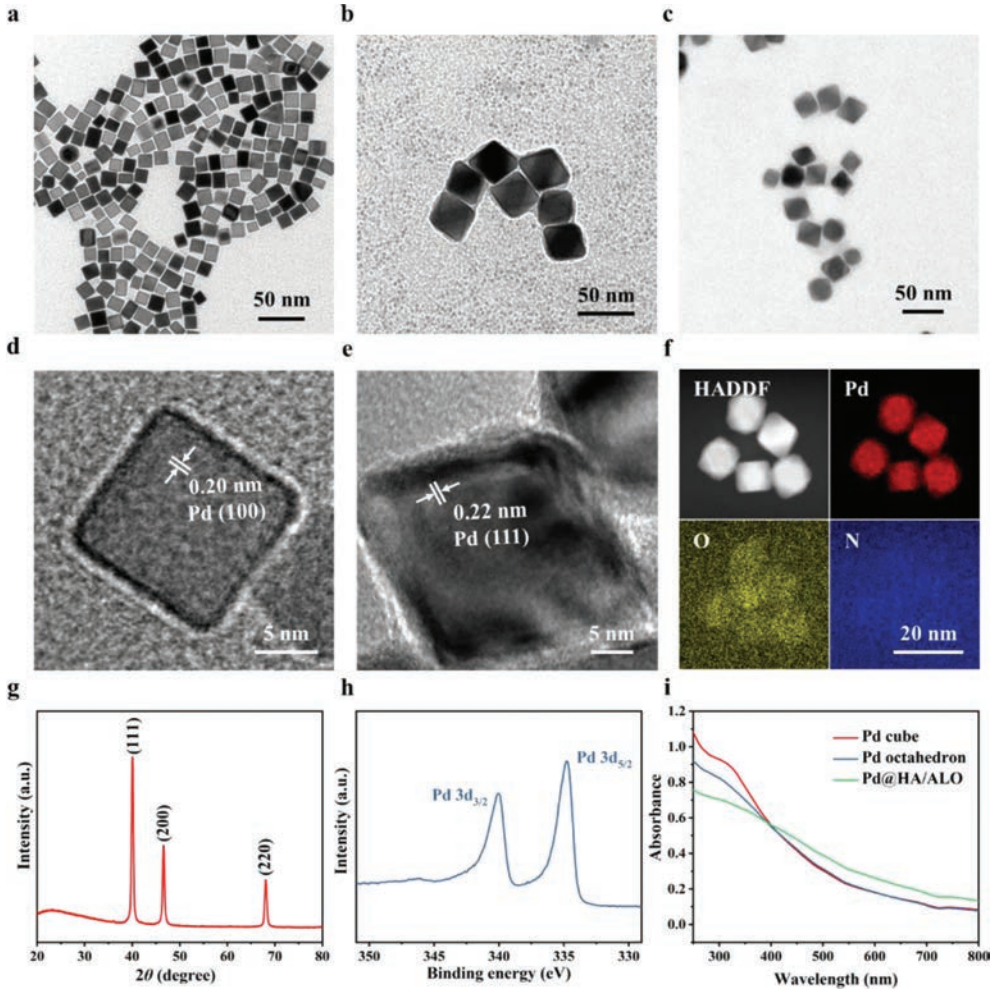

Fig. 1. Preparation and characterization of the Pd@HA/ALO. (a) TEM image of Pd nanocubes. (b) TEM image of Pd octahedrons. (c) TEM image of Pd@HA/ALO. (d) HRTEM image of Pd nanocubes. (e) HRTEM image of Pd octahedrons. (f) Element mapping of Pd@HA/ALO. (g) XPS spectra of Pd@HA/ALO. (h) XRD patterns of Pd@HA/ALO. (i) UV-vis spectra of Pd cubes, Pd octahedrons and Pd@HA/ALO.

to NIR window (Fig. 1i), suggesting the potential of Pd@HA/ALO to serve as a photothermal material. Additionally, the stability of Pd@HA/ALO was investigated in water, phosphate-buffered saline (PBS, pH 7.4), Dulbecco's modified Eagle's medium (DMEM) and fetal bovine serum (FBS). After 5 days, the size and dispersion properties of Pd@HA/ALO were well maintained, demonstrating that Pd@HA/ALO was stable enough for relatively long storage (Fig. S3 and Table S2 in Supporting information).

We further assessed the release kinetics of ALO from Pd@HA/ALO-based drug delivery systems *in vitro*. First, we detected the photothermal effect of Pd@HA/ALO upon 808 nm laser irradiation. As shown in Fig. 2a, the Pd@HA/ALO solution exhibited a concentration-dependent temperature increase with a maximum temperature of 43.8 °C under 808 nm laser irradiation, which was monitored by an IR camera (Fig. 2b). Moreover, the photothermal conversion efficiency of Pd@HA/ALO was determined to be 27.83% (Fig. 2c), indicating its excellent photothermal conversion properties. Then, we used NIR light to trigger the release of ALO from Pd@HA/ALO. Without the 808 nm laser, the amount of released ALO in pH 7.4 buffer was only 9.1% and 10.0% at 12 and 24 h, respectively (Fig. S4 in Supporting information). In contrast, after exposure to an 808 nm laser, the release percentage increased to 28.5% at 12 h and further reached 30.3% at 24 h, revealing that the NIR laser could efficiently control the release of ALO. This phenomenon is plausibly due to the rapid increase in local temperature generated from Pd@HA/ALO that increases the thermal vibration to weaken the interactions between ALO and Pd@HA to accelerate the release of ALO [42,43].

To investigate the ROS scavenging abilities of Pd@HA/ALO, we detected two representatives of ROS, H_2O_2 and superoxide anion ($O_2^{\bullet-}$). As expected, Pd@HA/ALO possessed high H_2O_2 scavenging activity in a concentration- and time-dependent manner (Fig. 2d and Fig. S5 in Supporting information). Specifically, more than 70% of H_2O_2 was eliminated within 5 min after exposure to 100 μg/mL Pd@HA/ALO. In addition, the CAT-like activity of Pd@HA/ALO (100 μg/mL) to scavenge H_2O_2 was approximately equal to that of 9.47 ± 0.61 U/mL CAT (Fig. 2e). Furthermore, typical EPR spectra were chosen to confirm the effect of Pd@HA/ALO on scavenging H_2O_2. The characteristic signal intensities of H_2O_2 were reduced with increasing Pd@HA/ALO concentrations and incubation times, revealing the excellent H_2O_2 scavenging capacity of Pd@HA/ALO (Figs. 2f and g).

Subsequently, we focused on the $O_2^{\bullet-}$ scavenging ability of Pd@HA/ALO. In this study, the $O_2^{\bullet-}$ concentration was reduced with increasing Pd@HA/ALO concentration and incubation time (Fig. 2h and Fig. S6 in Supporting information). Specifically, approximately 60% of the $O_2^{\bullet-}$ was decomposed after treatment with 200 μg/mL Pd@HA/ALO. In addition, the SOD-like activity of Pd@HA/ALO was shown to be concentration-dependent (Fig. 2i). The $O_2^{\bullet-}$ scavenging efficiency of Pd@HA/ALO (200 μg/mL) was

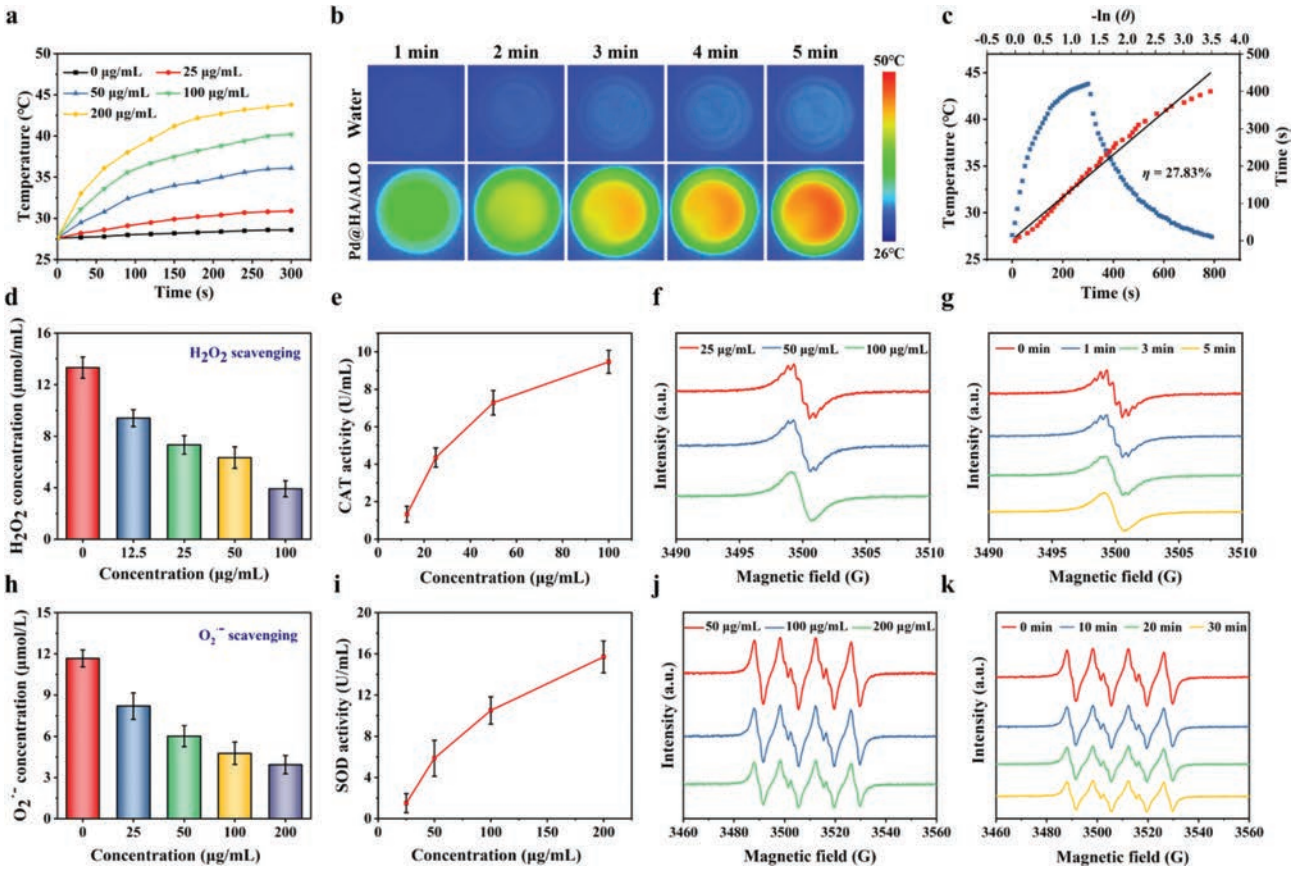

Fig. 2. Photothermal effect and multienzyme-like antioxidative activities of Pd@HA/ALO. (a) Temperature curves of different concentrations of Pd@HA/ALO in 5 min under 808 nm laser irradiation (1.0 W/cm^2). (b) Photothermal images of water and Pd@HA/ALO under 808 nm laser irradiation (1.0 W/cm^2). (c) Linear correlation of the cooling times *versus* negative natural logarithm of driving force temperature. (d) H_2O_2 scavenging ability after treated with different concentrations of Pd@HA/ALO for 5 min. (e) The CAT-like activity of Pd@HA/ALO. Data are mean ± SD ($n = 3$). (f) Concentration-dependent EPR spectra of Pd@HA/ALO for H_2O_2 scavenging. (g) Time-dependent EPR spectra of Pd@HA/ALO for H_2O_2 scavenging. (h) $O_2^{\bullet-}$ scavenging ability after treated with different concentrations of Pd@HA/ALO for 30 min. (i) SOD-like activity of Pd@HA/ALO. Data are mean ± SD ($n = 3$). (j) Concentration-dependent EPR spectra of Pd@HA/ALO for $O_2^{\bullet-}$ scavenging. (k) Time-dependent EPR spectra of Pd@HA/ALO for $O_2^{\bullet-}$ scavenging.

determined to be approximately equal to that of 15.70 ± 1.55 U/mL SOD. Moreover, the EPR spectra further demonstrated that Pd@HA/ALO exhibited a high $O_2^{\bullet-}$ scavenging capacity (Figs. 2j and k). Overall, these results confirmed that Pd@HA/ALO provided dual enzyme-like activity (SOD and CAT) to scavenge ROS, which is highly beneficial for antioxidative-based therapeutic interventions.

Encouraged by the outstanding ROS scavenging ability of Pd@HA/ALO, we next studied its biocompatibility *in vitro*. First, we assessed the hemocompatibility of Pd@HA/ALO after incubation with erythrocytes (Fig. 3a). No significant hemolysis (approximately 10%) of Pd@HA/ALO was observed even when the concentration was 200 μg/mL, which is in line with a negative surface charge of Pd@HA/ALO. Subsequently, analyses of cytotoxicity in RAW264.7 cells showed that Pd@HA/ALO induced only negligible cytotoxicity even at the maximum concentration (200 μg/mL), suggesting excellent cytocompatibility (Fig. 3b). Notably, Pd@HA/ALO induced slight cytotoxicity after exposure to the NIR laser due to induced hyperthermia (Fig. 3c).

Subsequently, we investigated the cellular uptake behavior of Pd@HA/ALO using confocal microscopy and TEM. For this purpose, RAW264.7 macrophages were incubated with fluorescein isothiocyanate (FITC)-labeled Pd@HA/ALO for 1, 3, 6, 9 and 12 h. Spatial FITC fluorescence (green color) exhibited a gradually increasing trend and reached a maximum at 9 h, confirming the successful cellular internalization of Pd@HA/ALO (Fig. 3d and Fig. S7 in Supporting information). According to the colocalization analysis, although the green fluorescence signals were largely co-localized with the red color of LysoTracker after 9 h of incubation (Pearson's correlation coefficient 0.55 ± 0.02), separated green fluorescence was observed at 12 h (Pearson's correlation coefficient 0.39 ± 0.05), indicating that the Pd@HA/ALO could effectively achieve endolysomal escape after internalization (Fig. S8 in Supporting information). Furthermore, after 12 h, penetration of the endolysosomal membrane by Pd@HA/ALO was observed leading to the release of Pd@HA/ALO into the cytoplasm (Fig. 3e). Therefore, these results confirmed that Pd@HA/ALO could be endocytosed effectively by RAW264.7 macrophages, which is a crucial prerequisite for a successful treatment of atherosclerosis.

Compared with other cells, during atherosclerosis, macrophages are more susceptible to oxidative stress. Therefore, the macrophage-mediated protection against ROS-induced oxidative damage and subsequent initiation of a cascade of pathological processes during the early stage of atherosclerosis significantly attenuate its progression. Thus, we further examined antioxidative activity of Pd@HA/ALO in RAW264.7 macrophages. As shown in the calcein-AM and propidium iodide (PI) co-staining assays, the addition of Pd@HA/ALO led to an efficient inhibition of induction of apoptosis triggered by H_2O_2 treatment (Fig. 3f). Subsequently, flow cytometric analysis was performed to further validate the cytoprotective ability of Pd@HA/ALO (Fig. 3g). Compared with that of the model group, a higher viable proportion (84.1%) and a lower apoptotic proportion (5.2%) of RAW264.7 macrophages were achieved after Pd@HA/ALO + NIR treatment, which is consistent with the results of the calcein-AM/PI co-staining.

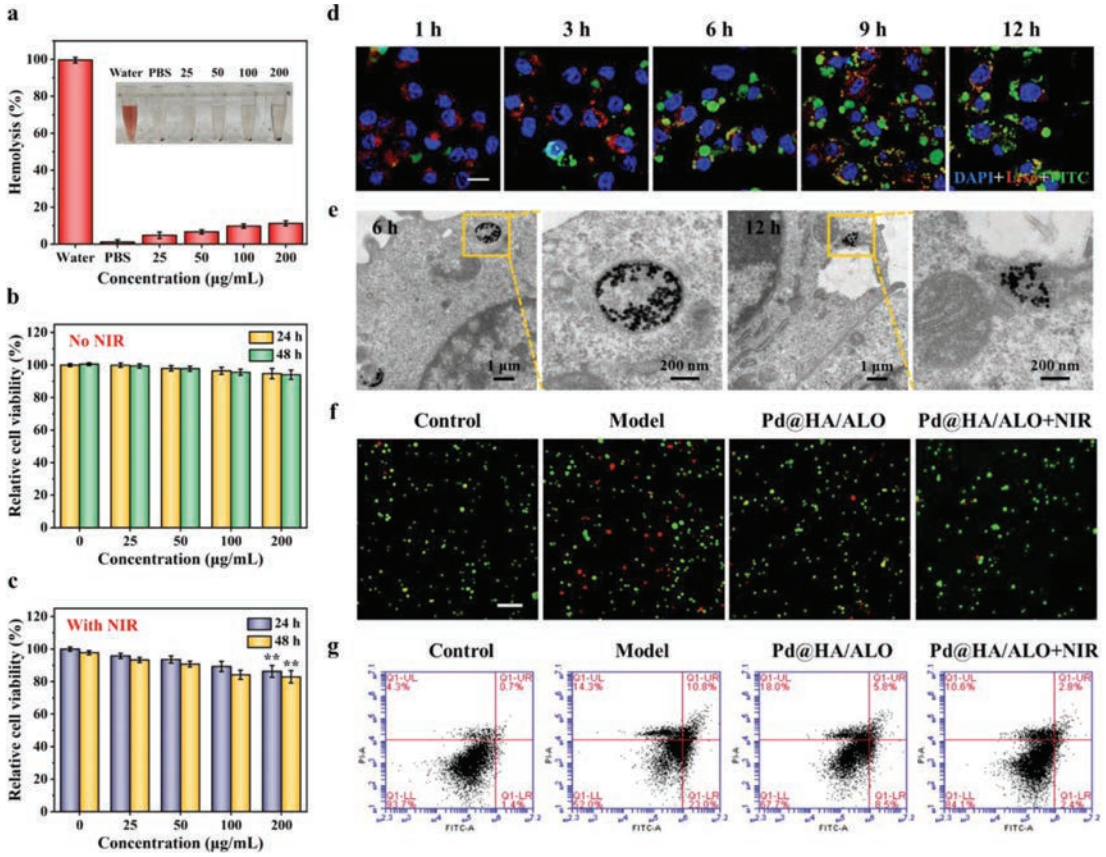

Fig. 3. *In vitro* cytotoxicity, cellular internalization and antioxidation of Pd@HA/ALO. (a) Hemolysis of red blood cells after incubation with different concentrations of Pd@HA/ALO for 2 h. Inset: hemolysis photograph after centrifugation. Data are mean ± SD ($n = 3$). (b) Relative cell viability of RAW264.7 cells after treated with different concentrations of Pd@HA/ALO without NIR laser irradiation for 24 and 48 h. (c) Relative cell viability of RAW264.7 cells after treated with different concentrations of Pd@HA/ALO with NIR laser irradiation for 24 and 48 h. Data are mean ± SD ($n = 5$). $^{**}P < 0.01$. (d) CLSM images of time-dependent cellular uptake of FITC-labeled Pd@HA/ALO. Scale bar: 10 μm. (e) Representative bio-TEM images of RAW264.7 cells after incubated with Pd@HA/ALO for 6 and 12 h. (f) CLSM images of calcein-AM and PI co-staining RAW264.7 cells after different treatments. Scale bar: 100 μm. (g) Flow cytometry analysis of RAW264.7 cells after different treatments.

Further, we also studied the direct *in vitro* ROS scavenging activity of Pd@HA/ALO in RAW264.7 cells. As shown in Fig. 4a, the intracellular total ROS (green fluorescent signal), H_2O_2 (green fluorescent signal) and $O_2^{\bullet-}$ (red fluorescent signal) levels increased dramatically after LPS treatment. Comparatively, the intracellular fluorescent signals of total ROS, H_2O_2 and $O_2^{\bullet-}$ decreased significantly when the cells were incubated with Pd@HA/ALO. Notably, after irradiation with an NIR laser, RAW264.7 cells in the Pd@HA/ALO group presented lower free radical fluorescence than those without irradiation (Figs. S9-S11 in Supporting information). Quantitative analysis of intracellular total ROS levels *via* flow cytometry further confirmed this observation (Fig. 4b). Taken together, these results demonstrate that Pd@HA/ALO nanoparticles significantly reduce intracellular ROS levels and protect RAW264.7 macrophages against ROS-induced oxidative damage.

Subsequently, we also investigated whether Pd@HA/ALO possessed an anti-inflammatory effect in macrophages. As shown in Fig. 4c, LPS-stimulated RAW264.7 cells showed significantly increased mRNA expression of COX-2, which plays a crucial role in the inflammatory behavior of activated macrophages. In contrast, the expression level of COX-2 was decreased after Pd@HA/ALO + NIR treatment, suggesting that the released ALO prominently inhibited COX-2 expression. Consequently, our results verified that Pd@HA/ALO could attenuate oxidation and inflammation in macrophages by inhibiting intracellular ROS and COX-2 production, respectively.

We next evaluated the *in vitro* macrophage polarization (M1 to M2 phenotypic transition) after incubation with Pd@HA/ALO. As shown in Fig. 4c, qRT-PCR analysis indicated that mRNA expression of proinflammatory M1 markers, including TNF-α, IL-1β and IL-6, was significantly increased after treatment with LPS. However, compared with the Pd@HA/ALO group, the Pd@HA/ALO + NIR group showed substantially reduced expression levels of proinflammatory M1 markers, indicating the increased release of ALO by NIR-induced hyperthermia. Moreover, the expression of representative M2 markers, including Arg-1 and CD206, was upregulated in the Pd@HA/ALO treatment group compared with the other groups. This results verified that Pd@HA/ALO could successfully promote the M1 to M2 phenotypic transition of macrophages through synergistic antioxidant and anti-inflammatory effects.

Subsequently, we explored the inhibitory effect of Pd@HA/ALO treatment on foam cell formation. For this purpose, RAW264.7 macrophages treated with 50 μg/mL oxLDL for 24 h presented many intracellular lipid droplets and significant foam cell formation, as illustrated by staining with Oil Red O (ORO) (Fig. 4d). Compared with the model group, the Pd@HA/ALO group showed notably suppressed foam cell formation, especially after NIR irradiation. Quantification of intracellularly deposited ORO supported this microscopic observation ($P < 0.01$) (Fig. 4e). Taken together, these results demonstrated that Pd@HA/ALO could suppress the formation of foam cells by inducing phenotypic alteration of macrophages from M1 to M2.

To study the anti-atherosclerotic effects *in vivo*, we first investigated the pharmacokinetic profiles of Pd@HA/ALO in C57BL/6 mice. All animal care and experimental protocols were approved by The Animal Ethics Committee of the Chinese Academy of Medical Sci-

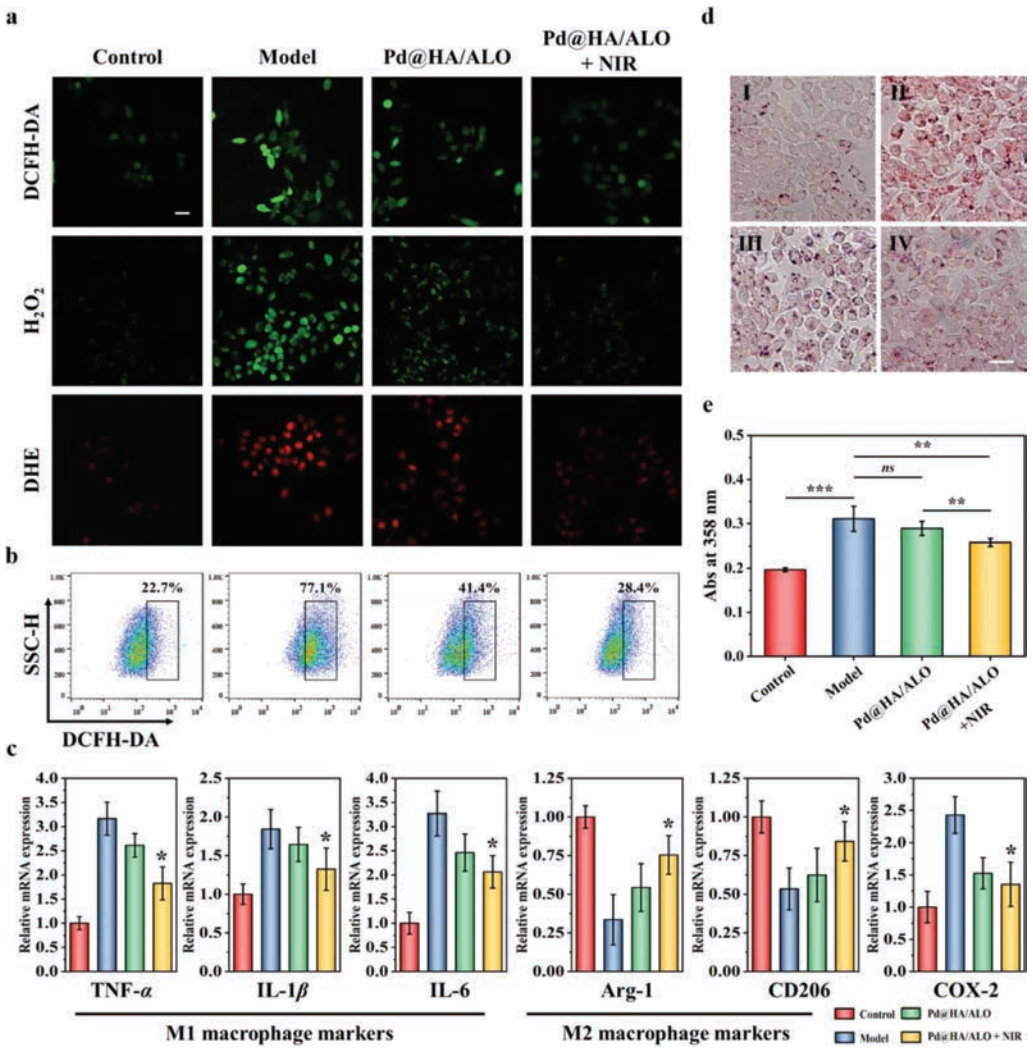

Fig. 4. Effect of Pd@HA/ALO on antioxidation, anti-inflammation and foam cell formation. (a) CLSM images showing intracellular ROS of RAW264.7 cells after different treatments. Intracellular total ROS, H_2O_2 and $O_2^{\bullet-}$ were stained by DCFH-DA, H_2O_2 probe and DHE, respectively. Scale bar: 20 μm. (b) ROS levels of RAW264.7 cells after different treatments. (c) mRNA expression of M1 (TNF-α, IL-1β, and IL-6), M2 (Arg-1 and CD206) macrophage markers and COX-2 in RAW264.7 cells after different treatments, as evaluated by qRT-PCR analysis. Data are mean ± SD ($n = 3$). $^{*}P < 0.05$. (d) Optical microscopy images showing oxLDL-induced foam cell formation in RAW264.7 cells after different treatments. I: Control; II: Model; III: Pd@HA/ALO; IV: Pd@HA/ALO + NIR. Scale bar: 50 μm. (e) Quantified contents of ORO in foam cells derived from RAW264.7 cells after different treatments. Data are mean ± SD ($n = 3$). $^{**}P < 0.01$, $^{***}P < 0.001$, ns: no significance.

ences Institute of Radiology. After i.v. injection, fluorescence imaging results suggested that the signal of ZnPc-labeled Pd@HA/ALO increased with time (Figs. 5a and b). This trend was different from the standard exponential damping of i.v. injected drugs, which was mainly reflected the non-linear profile of fluorescence signal accumulation and fluorescent substance decay. Then, we investigated the *in vivo* targeting ability in atherosclerotic plaque-bearing *ApoE*$^{-/-}$ mice. After i.v. injection for 4 h, fluorescence imaging showed that ZnPc-labeled Pd@HA/ALO accumulated in isolated entire aortas (Fig. 5c). At 12 h post-injection, imaging showed significantly stronger fluorescent signals in the isolated aortas, indicating that Pd@HA/ALO could target atherosclerotic plaques (Figs. 5c and d). Moreover, the accumulation of Pd@HA/ALO in major organs, including the heart, liver, spleen, lung, and kidneys, showed a time-dependent profile (Figs. S12 and S13 in Supporting information). In addition, the ability of Pd@HA/ALO to target atherosclerotic aortas was further demonstrated by immunofluorescence analysis. In this study, fluorescence imaging showed the substantial distribution of ZnPc-labeled Pd@HA/ALO in the aortic root and aortic arch (Fig. 5e, Figs. S14 and S15 in Supporting information). In particular, the red fluorescence (ZnPc) of Pd@HA/ALO displayed relatively high colocalization with the green fluorescence of CD68^{+} macrophages and CD31^{+} endothelial cells, revealing that the HA modification enhanced the atherosclerotic plaque-targeting capability *in vivo*. Thus, Pd@HA/ALO with targeted drug delivery allowed subsequent local drug release and efficient atherosclerosis management, resulting from decreased phagocytosis and sustained local drug release.

In addition, the ability of Pd@HA/ALO to target atherosclerotic aortas was further demonstrated by immunofluorescence analysis. In this study, fluorescence imaging showed the substantial distribution of ZnPc-labeled Pd@HA/ALO in the aortic root and aortic arch (Fig. 5e, Figs. S14 and S15). In particular, the red fluorescence (ZnPc) of Pd@HA/ALO displayed relatively high colocalization with the green fluorescence of CD68^{+} macrophages and CD31^{+} endothelial cells, revealing that the HA modification enhanced the atherosclerotic plaque-targeting capability *in vivo*. Thus, Pd@HA/ALO with targeted drug delivery allowed subsequent local drug release and efficient atherosclerosis management, resulting from decreased phagocytosis and sustained local drug release.

After confirming the significant accumulation of Pd@HA/ALO within plaques, we assessed the therapeutic effect in *ApoE*$^{-/-}$ mice. *ApoE*$^{-/-}$ mice were fed a high-fat diet for 10 weeks. At 1 week,

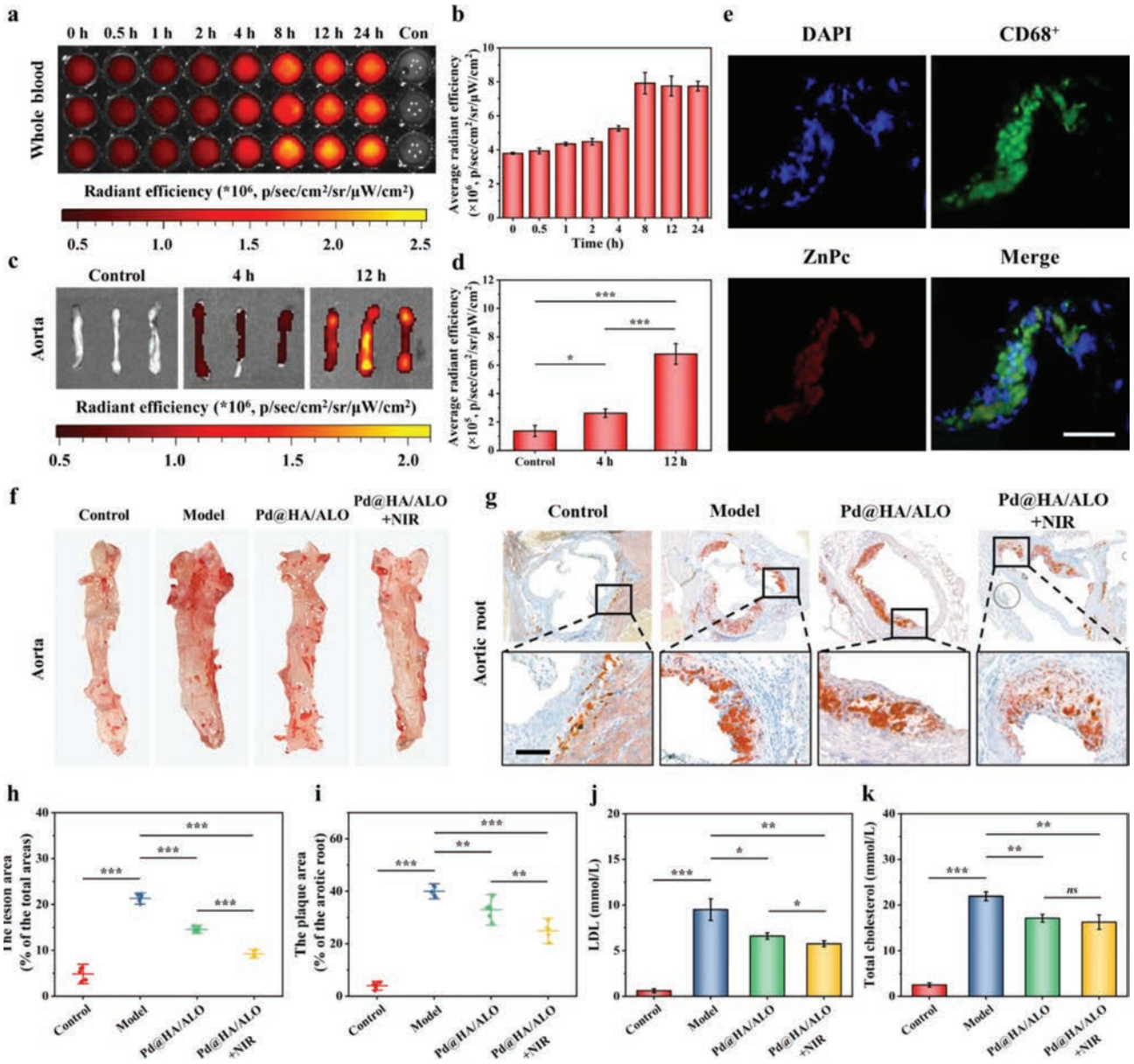

Fig. 5. *In vivo* targeting ability and therapeutic effects of Pd@HA/ALO. (a) *Ex vivo* images of whole blood collected at various time points after i.v. administration of ZnPc-labeled Pd@HA/ALO. (b) Quantified data of fluorescence intensities. Data are mean ± SD ($n = 3$). (c) *Ex vivo* fluorescence images and (d) quantitative data of fluorescence signals accumulated in the aorta at 4 and 12 h points after i.v. administration of ZnPc-labeled Pd@HA/ALO. Data are mean ± SD ($n = 3$). (e) Immunofluorescence analysis of the colocalization of ZnPc-labeled Pd@HA/ALO with $CD68^+$ macrophages in the aortic root. Scale bar: 100 μm. (f) Representative ORO-stained images of aortas in each group. (g) Representative ORO-stained images of aortic roots sections in each group. Scale bar: 100 μm. (h) Quantitative data of the atherosclerotic plaque area. (i) Quantitative data of the atherosclerotic plaque area in the aortic root sections. Data are mean ± SD ($n = 5$). (j) Serum levels of LDL in $ApoE^{-/-}$ mice after different treatments. (k) Serum levels of total cholesterol in $ApoE^{-/-}$ mice after different treatments. Data are mean ± SD ($n = 3$). $^*P < 0.05$, $^{**}P < 0.01$, $^{***}P < 0.001$, ns: no significance.

the animals were randomized into 4 groups with different treatments: control (C57BL/6 mice), model (saline), Pd@HA/ALO (10 mg/kg) and Pd@HA/ALO (10 mg/kg) + NIR. Mice received twice-weekly i.v. injections for a total of 10 weeks. After treatment, the whole aortas were harvested and stained with ORO. Atherosclerotic lesions identified by ORO staining were present in the model group, and the lesion area of the plaque in the Pd@HA/ALO treatment group was significantly reduced compared with that of the model group (Fig. 5f). Importantly, the highest decrease in the ORO-stained areas in aortas was observed for the mice in the NIR irradiation group. Consistent with this result, the ORO-stained cryosections from the aortic root also revealed the extent of plaque reduction in the vascular lumen (Fig. 5g). Further quantification of the ORO-stained plaques showed that the ratio of the plaque area to that of the whole aorta was decreased from 21.29% to 14.56% after treatment with Pd@HA/ALO (Fig. 5h). In addition, Pd@HA/ALO + NIR treatment achieved a significantly higher therapeutic efficacy, as shown by a plaque ratio of 9.24%, revealing that the NIR-triggered release of ALO strongly inhibits atherosclerotic development. Compared with that of the model group (40.00%), the plaque area ratio decreased to 32.93% and 24.90% after treatment with Pd@HA/ALO and Pd@HA/ALO + NIR, respectively (Fig. 5i), confirming that Pd@HA/ALO could effectively attenuate the progression of atherosclerosis.

Subsequently, the composition of atherosclerotic plaques in aortic root sections was detected by H&E staining and immunohistochemistry. Examination of the H&E-stained sections of aortic roots showed that plaques in the model group largely consisted

of acellular and lipid-rich necrotic cores (Fig. S16a in Supporting information). After treatment with Pd@HA/ALO, the necrotic area was notably decreased. Specifically, the quantitative analysis indicated that the necrotic core area was decreased from 26.86% to 16.42% after treatment with Pd@HA/ALO + NIR (Fig. S16b in Supporting information). Further separate immunohistochemical analyses for CD68 (a macrophage marker) and MMP-9 indicated that the number of macrophages and the level of MMP-9 were dramatically reduced in the atherosclerotic plaque area after treatment with Pd@HA/ALO, particularly after NIR irradiation (Figs. S17a-c in Supporting information). These findings indicated that Pd@HA/ALO can effectively suppress the progression of atherosclerosis due to the blockade of macrophage infiltration and the stabilization of vulnerable plaques. Concordant with these findings, staining with Masson's trichrome showed a higher content of collagen around plaques of the Pd@HA/ALO-treated groups, resulting in enhanced fibrous cap thickness (Figs. S17a and d in Supporting information). Moreover, the immunohistochemical analyses for α-SMA (an SMC marker) demonstrated a high accumulation of SMCs in plaques in the Pd@HA/ALO-treated groups, indicating that vascular SMC proliferation was beneficial at various stages of atherogenesis (Figs. S17a and e in Supporting information) [44]. Accordingly, these results demonstrated that Pd@HA/ALO lowers the accumulation of macrophages in plaques, prevent the formation of vulnerable plaques and increase the number of SMCs, thereby effectively delaying the development of atherosclerosis.

Finally, the possible adverse effects of Pd@HA/ALO were examined after 10 weeks treatment. The clinical biochemical analysis of ALT, AST, ALP, BUN and CREA revealed normal values, suggesting that the functions of the liver and kidney were barely impaired after treatment with different formulations (Fig. S18 in Supporting information). Additionally, the levels of HDL, LDL, TGs and TC were examined. Compared to the model groups, the Pd@HA/ALO and Pd@HA/ALO + NIR groups displayed lower levels of LDL and TC, whereas no distinguishable changes were found in the TGs and HDL levels (Fig. S18, Figs. 5j and k). In addition, examination of H&E-stained sections of major organs (heart, liver, spleen, lung and kidney) showed no obvious tissue pathologies in the treated mice of all groups, which further confirmed the good biocompatibility of Pd@HA/ALO (Fig. S19 in Supporting information). Together, these findings indicated that Pd@HA/ALO possessed a good safety profile for long-term treatment.

In summary, we successfully engineered an endogenous targeted Pd@HA/ALO nanozyme to enhance macrophage polarization (M1 to M2) for treatment of atherosclerosis. Pd@HA/ALO innately exhibited multiple antioxidant enzyme activities to degrade intracellular ROS, leading to an antioxidative effect. Moreover, the ALO released from Pd@HA/ALO inhibited the expression of COX-2, which further relieved the inflammatory state. Synergistic antioxidant and anti-inflammatory effects effectively promoted the polarization of macrophages from the M1 to M2 subtype, thus suppressing the formation of foam cells. Furthermore, Pd@HA/ALO displayed a desirable safety profile without notable side effects, even after long-term administration in mice. Overall, Pd@HA/ALO could be a blueprint for next-generation nanomedicine in cardiovascular disease treatment and prevention.

Declaration of competing interest

The authors declare that they have no known competing financial interests or personal relationships that could have appeared to influence the work reported in this paper.

Acknowledgments

This work was supported by the Young Elite Scientists Sponsorship Program by Tianjin (No. 0701320001) and the Major Special Projects (No. 0402080005). Furthermore, the financial support from the CEITEC 2020 Project (No. LQ1601) and the Ministry of Education, Youth and Sports of the Czech Republic under the National Sustainability Programme II and by ERDF (No. CZ.02.1.01/0.0/0.0/16_025/0007314) is highly acknowledged.

Supplementary materials

Supplementary material associated with this article can be found, in the online version, at doi:10.1016/j.cclet.2022.06.008.

References

[1] P. Libby, Thromb. Arterioscler, Vasc. Biol. 32 (2012) 2045–2051.
[2] H. Hemingway, F.W. Asselbergs, J. Danesh, et al., Eur. Heart J. 39 (2018) 1481–1495.
[3] Y. Song, H. Jing, L.B. Vong, J. Wang, N. Li, Chin. Chem. Lett. 33 (2022) 1705–1717.
[4] P.D. Thompson, G. Panza, A. Zaleski, et al., J. Am. Coll. Cardiol. 67 (2016) 2395–2410.
[5] R.J. Andrade, N. Chalasani, E.S. Björnsson, et al., Nat. Rev. Dis. Primers 5 (2019) 1–22.
[6] Y. Sawayama, C. Shimizu, N. Maeda, et al., J. Am. Coll. Cardiol. 39 (2002) 610–616.
[7] S.R. Thomas, P.K. Witting, R. Stocker, et al., BioFactors 9 (1999) 207–224.
[8] S. Mora, J.A.E. Manson, JAMA Intern. Med. 176 (2016) 1195–1204.
[9] M.E. Burleigh, V.R. Babaev, M.B. Patel, et al., Biochem. Pharmacol. 70 (2005) 334–342.
[10] I. Tabas, K.E. Bornfeldt, Circ. Res. 118 (2016) 653–667.
[11] G. Chinetti-Gbaguidi, S. Colin, B. Staels, Nat. Rev. Cardiol. 12 (2015) 10–17.
[12] K.J. Moore, I. Tabas, Cell 145 (2011) 341–355.
[13] A. Laria, A. Lurati, M. Marrazza, et al., J. Inflammation Res. 9 (2016) 1–11.
[14] B. Kim, H.B. Pang, J. Kang, et al., Nat. Commun. 9 (2018) 1969.
[15] Y. Song, Y. Huang, F. Zhou, J. Ding, W. Zhou, Chin. Chem. Lett. 33 (2022) 597–612.
[16] K.J. Moore, F.J. Sheedy, E.A. Fisher, Nat. Rev. Immunol. 13 (2013) 709–721.
[17] M. Bäck, A.Y. Jr, I. Tabas, K. Öörni, P.T. Kovanen, Nat. Rev. Cardiol. 16 (2019) 389–406.
[18] H.B. Cohen, D.M. Mosser, J. Leukocyte Biol. 94 (2013) 913–919.
[19] C. Yunna, H. Mengru, W. Lei, C. Weidong, Eur. J. Pharmacol. 877 (2020) 173090.
[20] R. Rajakariar, M.M. Yaqoob, D.W. Gilroy, Mol. Interventions 6 (2006) 199.
[21] L. Minghetti, J. Neuropathol. Exp. Neurol. 63 (2004) 901–910.
[22] H. Wang, S. Yang, H. Zhou, et al., J. Hematol. Oncol. 8 (2015) 1–13.
[23] Y. Yang, S.J. Jin, H.L. Wang, et al., Scand. J. Pain 8 (2015) 28–34.
[24] P.U. Atukorale, G. Covarrubias, L. Bauer, E. Karathanasis, Adv. Drug Delivery Rev. 113 (2017) 141–156.
[25] J.W. Myerson, A.C. Anselmo, Y. Liu, et al., Adv. Drug Delivery Rev. 99 (2016) 97–112.
[26] M.D. Howard, E.D. Hood, B. Zern, et al., Annu. Rev. Pharmacol. Toxicol. 54 (2014) 205–226.
[27] A.M. Flores, J. Ye, K. Jarr, et al., Arterioscler. Thromb. Vasc. Biol. 39 (2019) 635–646.
[28] F. Dormont, M. Varna, P. Couvreur, Mater. Today 21 (2018) 122–143.
[29] D.R. Lewis, L.K. Petersen, A.W. York, et al., Proc. Natl. Acad. Sci. U. S. A. 112 (2015) 2693–2698.
[30] S. Sha, L.B. Vong, P. Chonpathompikunlert, et al., Biomaterials 34 (2013) 8393–8400.
[31] A. Eguchi, T. Yoshitomi, M. Lazic, et al., Nanomedicine 10 (2015) 2697–2708.
[32] C. Brenner, W.M. Franz, S. Kühlenthal, et al., Int. J. Cardiol. 199 (2015) 163–169.
[33] S. Yang, H.Q. Yuan, Y.M. Hao, et al., Clin. Chim. Acta 501 (2020) 142–146.
[34] H.Y. Tan, N. Wang, S. Li, et al., Oxid. Med. Cell. Longevity 2016 (2016) 2795090.
[35] Y. Yang, J. Wang, S. Guo, et al., Redox Biol. 32 (2020) 101501.
[36] A. Chen, C. Ostrom, Chem. Rev. 115 (2015) 11999–12044.
[37] M.A. Miller, B. Askevold, H. Mikula, et al., Nat. Commun. 8 (2017) 15906.
[38] G. Fang, W. Li, X. Shen, et al., Nat. Commun. 9 (2018) 129.
[39] J. Wu, X. Wang, Q. Wang, et al., Chem. Soc. Rev. 48 (2019) 1004–1076.
[40] C. Ge, G. Fang, X. Shen, et al., ACS Nano 10 (2016) 10436–10445.
[41] M. Jin, H. Zhang, Z. Xie, Y. Xia, Energy Environ. Sci. 5 (2012) 6352–6357.
[42] K. Yang, S. Zhang, G. Zhang, et al., Nano Lett. 10 (2010) 3318–3323.
[43] Z. Zhang, L. Wang, J. Wang, et al., Adv. Mater. 24 (2012) 1418–1423.
[44] M.R. Bennett, S. Sinha, G.K. Owens, Circ. Res. 118 (2016) 692–702.